

Recyclable CoFe₂O₄-Ag₂O magnetic photocatalyst and its visible light-driven photocatalytic performance

Qihui Zeng¹ · Yingming Zhu¹ · Wen Tian¹ ·
Wei Jiang¹ · Bin Liang¹

Received: 8 November 2016 / Accepted: 2 February 2017
© Springer Science+Business Media Dordrecht 2017

Abstract A magnetically separable photocatalyst, the composite compound CoFe₂O₄-Ag₂O, was fabricated successfully by a simple precipitation method and used for photodegradation of organic pollutants under visible light (>420 nm) irradiation. Its magnetic separation performance was evaluated. Results showed that the CoFe₂O₄-Ag₂O with 60-wt% content of Ag₂O had the best photocatalytic performance, stability, and magnetic separation performance. Methyl orange, methylene blue, rhodamine B, and phenol can be completely photodegraded by the CoFe₂O₄-Ag₂O photocatalyst in a short period. After five cycles, CoFe₂O₄-Ag₂O kept its performance stability. As prepared, CoFe₂O₄-Ag₂O (60%) has a coercivity of 2500 Oe and a saturation magnetization of 22.45 emu g⁻¹; it can be completely separated magnetically in 20 s with magnetic recovery mass rate of 85% under an external magnetic field. This superb photocatalytic performance and separation recovery confirms that the CoFe₂O₄-Ag₂O photocatalyst is a promising candidate for future use in photo-oxidative degradation of organic contaminants.

Keywords Cobalt ferrite · Silver oxide · Visible light · Photocatalyst · Magnetic separation

Introduction

Increasing demand for and shortage of clean water sources have become burning issues with the progress of humankind. Various methods and techniques have been proposed to address these issues [1–7]. Among them, photocatalytic oxidation is

✉ Wei Jiang
weijiang@scu.edu.cn

¹ Multi-Phases Mass Transfer and Reaction Engineering Laboratory, School of Chemical Engineering, Sichuan University, Chengdu 610065, China

considered an ideal environmental pollution control technology for color removal and destruction of persistent organic pollutants due to facile reaction conditions, no secondary pollution, and direct utilization of sunlight for oxidation reactions without extra energy consumption [8–11]. TiO_2 , a typical semiconductor, attracted attention as a photocatalyst due to its chemical stability, low cost, and nontoxicity [12]. However, the relatively wide band gap of TiO_2 (≈ 3.2 eV) limited its efficient utilization of solar energy [13]. Developing visible light-driven photocatalysts was an effective strategy for practically applying photocatalytic oxidation.

Currently, silver compounds like Ag_3PO_4 [14, 15], Ag_2CO_3 [16, 18], Ag_3AsO_4 [19], AgX ($X = \text{Cl}, \text{Br}, \text{I}$) [20–22], Ag_2S [23], and Ag_2O [24, 25] have exhibited superb photocatalytic abilities under visible light irradiation. Typical organic pollutants such as methyl orange (MO), methylene blue (MB), rhodamine B (RhB), and phenol can be photodecomposed in a short time [17]. Ag_2O can photodegrade MO completely in 120 s under sunlight irradiation and maintain excellent photocatalytic activity after six cycles [24]. These facts demonstrate the promising future of silver compounds, especially Ag_2O , for use as highly efficient photocatalysts.

The expense and potential pollution risk posed by Ag_2O use require its recovery and reuse; however, initial separation of nanoparticulate Ag_2O from suspension was energy-consuming and expensive due to the size of the nanoparticles [26]. Three energy-efficient strategies were adopted to solve the separation problem of nanoparticles: immobilization [27], loading on a support [28, 29], and magnetic separation [30–32]. The first two approaches decreased the difficulty in separation, but photocatalytic performance decreased due to loss of surface area from aggregation, loading or coating on supports. Comparably, magnetic separation is more attractive because the photocatalyst component can be loaded or grown on small magnetic nanoparticle cores with relatively small loss in surface area. The photocatalyst forms the active surface layer on the magnetic cores only; hence, the amount of photocatalyst required is reduced because none is lost to the bulk. Therefore, the addition of magnetic particles to Ag_2O , which improves its separation efficiency without observable performance loss, is highly attractive.

Cobalt ferrite (CoFe_2O_4) has been widely used as a magnetic support because of its high coercivity, moderate saturation, and remarkable chemical stability [33]. CoFe_2O_4 nanoparticles have been used to fabricate CoFe_2O_4 –graphene composite photocatalysts, enhancing the photocatalytic efficiency and conducting magnetic separation in a suspension system [30]. Senapati et al. reported the synthesis of titania-coated CoFe_2O_4 by the polymeric precursor method, allowing easy separation of the photocatalysts after the oxidative process [34]. The heterostructure of CoFe_2O_4 embedded in one-dimensional ZnO photocatalyst showed high saturation magnetization, which indicated the possibility of recycling the nanostructure [35]. These reports confirmed that CoFe_2O_4 nanoparticles constitute an effective magnetic support for obtaining high separation efficiency, adequate surface area, and excellent photocatalytic performance.

In this study, a magnetically separable CoFe_2O_4 – Ag_2O photocatalyst was designed and fabricated by a simple precipitation method. Morphology and structure of the CoFe_2O_4 – Ag_2O was characterized, and its photocatalytic performance was

evaluated to determine the best hybrid ratio of the composite by photodegradation of MO, RhB, MB, and phenol. Its photocatalytic performance and improved separation efficiency were confirmed by repeating the photodegradation process of MO and through magnetic separation using an external magnetic field.

Materials and methods

Materials

All analytical-grade reagents, including AgNO₃, NaOH, ethanol, Fe(NO₃)₃·9H₂O, and Co(NO₃)₂·6H₂O, were purchased from ChengDu KeLong Chemical Reagent Co. Ltd. and used directly without further purification.

Synthesis of magnetic CoFe₂O₄–Ag₂O composite photocatalyst

CoFe₂O₄ nanoparticles were synthesized by the hydrothermal method. Fe(NO₃)₃·9H₂O (5 mmol) and Co(NO₃)₂·6H₂O (2.5 mmol) were dissolved in absolute ethanol (40 mL) to form a clear solution. An appropriate NaOH solution (80 mmol) was added to the solution until the pH reached 13. After being stirred vigorously for 30 min, the solution was transferred to a 100-mL Teflon-lined stainless autoclave and maintained at 80 °C for 20 h, and then allowed to cool to room temperature. The black precipitate was magnetically separated, washed three times with deionized (DI) water, and dried at 60 °C in air for 12 h to obtain the final CoFe₂O₄ product.

A simple precipitation process synthesized CoFe₂O₄–Ag₂O hybrid compounds with different Ag₂O content. To synthesize CoFe₂O₄–Ag₂O with 60 wt% Ag₂O content, 0.28 g CoFe₂O₄ nanoparticles and 0.6157 g AgNO₃ were added into 80 mL of deionized (DI) water with stirring for 2 h. 12 mL of NaOH (0.3 M) solution was titrated into the suspension at a dropping speed of 3.2 mL min⁻¹ and the suspension was stirred for 2 h until the initial black color changed to dark brown. The suspension was then magnetically separated with a permanent magnet. The separated solid was washed with DI water three times to dissolve any unreacted raw material or impurities, and dried overnight at 60 °C in air to obtain the final dark brown powder product.

Analytical methods

Crystal structures of the samples were determined using glancing-angle X-ray diffraction (XRD; DX-2007 SSC) with a Cu K α 40 kV/30 mA X-ray source ($\lambda = 0.15406$ nm). The X-ray photoelectron spectroscopy (XPS) data (chemical compositions and valence band spectra) were taken on an XSAM 800 instrument from Kratos using monochromatic Al K α radiation and a charge neutralizer. To compensate for surface charge effects, all binding energies were referenced to the C 1s peak (284.6 eV) arising from adventitious carbon. Scanning electron microscopy (SEM; JSM-7500F JEOL) and high-resolution transmission electron microscopy

(HRTEM; FEI Tecnai G2 F20 S-TWIN) were employed to observe the morphologies and microstructures. Particle size distribution was analyzed by an ab JL-6000 type dry and wet dual-purpose laser particle sizer. UV–visible diffusion reflection spectrometry (UV–Vis DRS) was performed using a UV–visible spectrophotometer (Alpha-1506) and fine-grained BaSO₄ powder as the standard. Surface areas of samples were determined by the nitrogen adsorption method with a Brunauer–Emmett–Teller (BET) analyzer (SSA-3500, Builder, China). The photoluminescence (PL) measurements were carried out on a fluorescence spectrometer (F-7000, Hitachi, Japan) at room temperature. Magnetic characterization was carried out with a homemade vibrating sample magnetometer. Magnetization curves were measured at room temperature after applying a maximum magnetic field of 5 T.

Organic dye decomposition

Photocatalytic activity of the samples was evaluated with an OCRS-IV photoreactor system, which included a 500-W Xe lamp and eight 50-mL quartz test tubes, a cut-off filter with a specified light wavelength (removes any radiation below 420 nm) and a water shelter. Photocatalytic evaluation testing was carried out in parallel by photodegrading organics under visible light illumination without any sacrificial reagents. Organics used for evaluation included MO (16 mg L⁻¹), RhB (16 mg L⁻¹), MB (8 mg L⁻¹), or phenol (25 mg L⁻¹) solutions.

In a typical process, 0.1 g of photocatalyst was dispersed in a 10 mL of solution by stirring in the dark, forming a suspension. Before illumination, the suspension was kept in the dark for 40 min to reach adsorption equilibrium. In some cases, such as photodegradation of MB and RhB, the adsorption step in the dark was omitted because the adsorption rate was significantly slower than the photocatalytic reaction. The suspension was then exposed under visible light irradiation with an agitation rate of 250 rpm. After a certain time, an aliquot of the suspension, from which the photocatalyst had been removed with a magnet, was used to determine its maximum absorbance peak with a TU-1901 UV–Vis spectrophotometer.

Recyclability of CoFe₂O₄–Ag₂O catalysts was also investigated. After each round of catalysis, the solid sample was magnetically collected and washed with DI water. After drying, the sample was used for subsequent photoreaction cycles.

Results and discussion

Catalyst characterization

The XRD diffraction patterns of pure Ag₂O, CoFe₂O₄, and CoFe₂O₄–Ag₂O hybrid are shown in Fig. 1. For pure Ag₂O and CoFe₂O₄, all the diffraction peaks determined were assigned by comparison to their corresponding standard materials, a cubic spinel-type CoFe₂O₄ (JCPDS 22-1086) and Ag₂O (JCPDS 41-1104) with cubic structure. The characteristic peaks of both materials can be observed in the spectrum of the CoFe₂O₄–Ag₂O hybrid shown in Fig. 1a. As shown in Fig. 1b, the diffraction peaks of Ag₂O are reinforced and CoFe₂O₄ are crosscurrent. All the

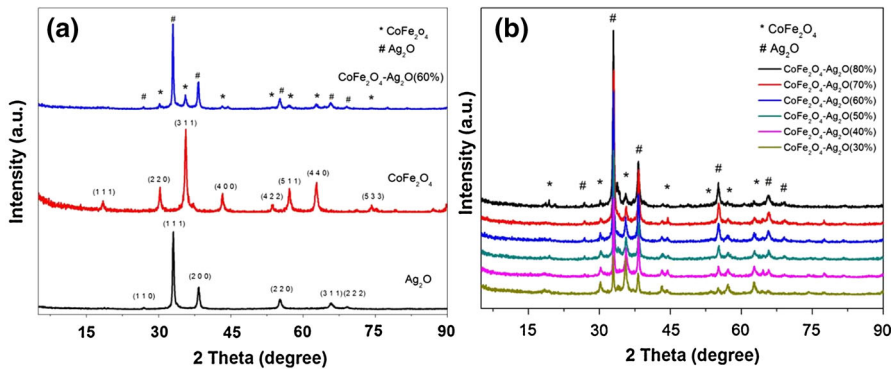


Fig. 1 a XRD patterns of the as-prepared CoFe₂O₄-Ag₂O (60%), CoFe₂O₄, Ag₂O. In the CoFe₂O₄-Ag₂O (60%), peaks marked with (*) correspond to CoFe₂O₄ and peaks marked with (#) correspond to Ag₂O. b XRD patterns of the as-prepared CoFe₂O₄-Ag₂O with different Ag₂O content (range 30–80%)

peaks appear without any significant deviation and no new peaks are observed. This means that no new substances are generated and no lattice distortions occur due to the interaction between Ag₂O and CoFe₂O₄; the obtained CoFe₂O₄-Ag₂O hybrid is a two-solid-phase mixture of pure Ag₂O and CoFe₂O₄.

Morphological structures of CoFe₂O₄ and CoFe₂O₄-Ag₂O (60%) are further observed by SEM and TEM (Fig. 2). The SEM image of CoFe₂O₄ (Fig. 2a) shows that the as-prepared CoFe₂O₄ magnetic particles have diameters of 30–50 nm, and are aggregates of cubic grains the size of ~15 nm. After introducing Ag₂O by precipitation, 5–10-nm grains deposited on the surface of the CoFe₂O₄ aggregation are observed, forming an encapsulated structure (Fig. 2b). No obvious cubic grain structures or their junctions are observed. The HRTEM images of the CoFe₂O₄-Ag₂O (60%) sample (Fig. 2c, d) confirm the existence of Ag₂O on magnetic support CoFe₂O₄. These show that the outer boundary of the hybrid appears different from the particle bulk; a number of dark shadows of small grains with diameter of ~5 nm adhere to the edge of giant grey particles. Lattice fringe images of small grains and bulk determined are 0.25 and 0.27 nm, which are in agreement with the lattice spaces of (311) of CoFe₂O₄ and (111) of Ag₂O, respectively. The determined morphology of CoFe₂O₄-Ag₂O (60%) reveals that the Ag₂O has tightly wrapped around the CoFe₂O₄ nanoparticle aggregation to form larger particles. The BET result of the CoFe₂O₄-Ag₂O (60%) sample is 24.6812 m³ g⁻¹, which is far larger than pure Ag₂O sample (2.3212 m³ g⁻¹), indicating a potential increase in photocatalytic performance.

Particle size distribution of CoFe₂O₄ and CoFe₂O₄-Ag₂O (60%) are determined and shown in Fig. 3. It can be found that the particle size of the composite sample, CoFe₂O₄-Ag₂O (60%), ranges from 400 nm to 2000 nm, which is remarkably larger than of the pure magnetic support, CoFe₂O₄, between 200 and 400 nm. This significant increase of particle size should be ascribed to the enwrapping of Ag₂O around the magnetic CoFe₂O₄ core. This result is in agreement to the SEM results above.

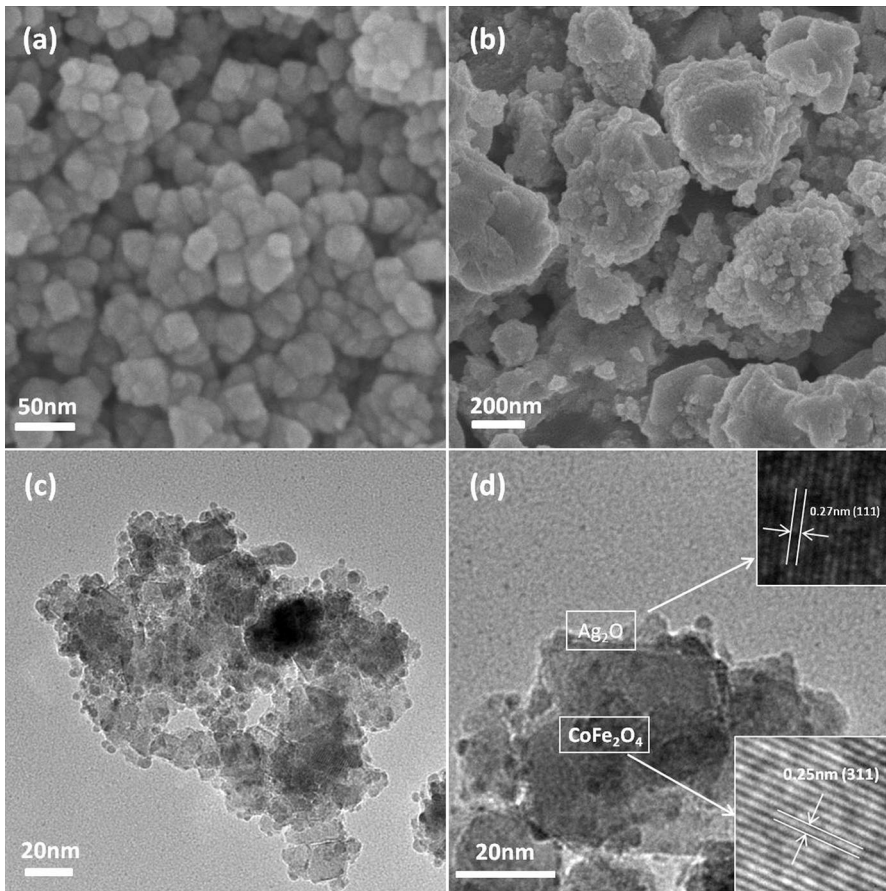


Fig. 2 SEM images of **a** CoFe_2O_4 and **b** $\text{CoFe}_2\text{O}_4\text{-Ag}_2\text{O}$ (60%). TEM **c**, **d** images of $\text{CoFe}_2\text{O}_4\text{-Ag}_2\text{O}$ (60%). The *inset* shows the lattice fringe images of Ag_2O and CoFe_2O_4 , respectively

The band gap energy of $\text{CoFe}_2\text{O}_4\text{-Ag}_2\text{O}$ was determined by UV-Vis DRS to investigate its electronic structure and possible interactions between CoFe_2O_4 and Ag_2O . The band gap energy was estimated according to Eq. (1):

$$E_g = 1240/\lambda \quad (1)$$

where E_g is the band gap of the semiconductor and λ is the threshold wavelength (the wavelength of the corresponding absorbance edge). The absorbance edge can be determined by the crossover point of an extended tangent line of the absorption curve and the x axis. Figure 4 shows that the threshold wavelength of pure Ag_2O is 941 nm, with a calculated band gap value of 1.31 eV. The band gap of pure CoFe_2O_4 is 1.34 eV, which corresponds well to previous studies [36]. The crossing point of the $\text{CoFe}_2\text{O}_4\text{-Ag}_2\text{O}$ (60%) hybrid is 931 nm, with an estimated band gap of 1.33 eV. This result confirms that there is no noticeable interaction between the magnetic support and the loaded active species, which is in accordance with the

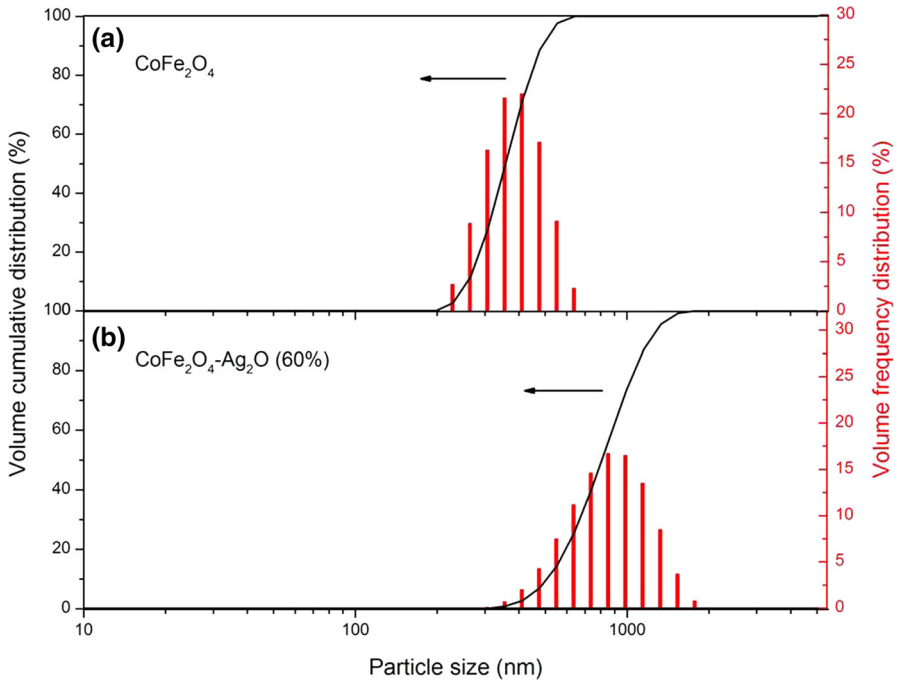


Fig. 3 Particle size distribution of **a** CoFe_2O_4 and **b** $\text{CoFe}_2\text{O}_4\text{-Ag}_2\text{O}$ (60%)

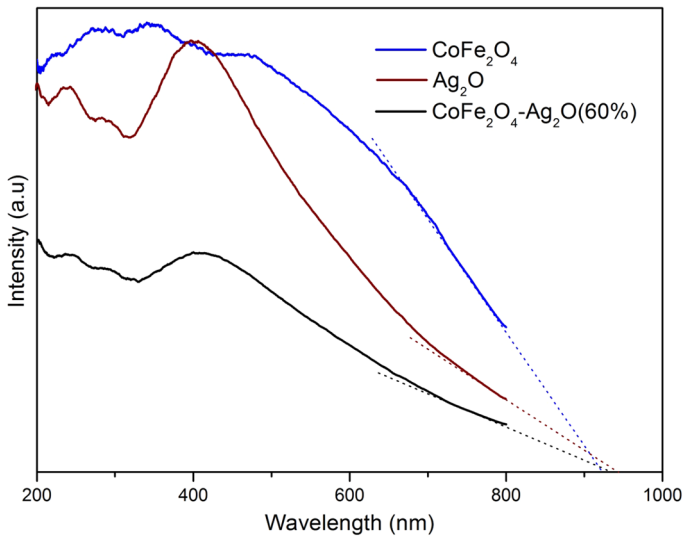


Fig. 4 UV-Vis diffusion reflection spectrometry of pure Ag_2O , CoFe_2O_4 and as-prepared $\text{CoFe}_2\text{O}_4\text{-Ag}_2\text{O}$ (60%) samples from 200 to 800 nm

XRD results. Ag_2O is only immobilized on the CoFe_2O_4 surface; therefore, no significant photocatalytic performance degradation should happen.

Photocatalytic evaluation

MO, a typical persistent organic compound, was selected as the main target to evaluate the photocatalytic performance of the $\text{CoFe}_2\text{O}_4\text{-Ag}_2\text{O}$ hybrids and to identify the optimal content of Ag_2O . Furthermore, other common organic pollutants like MB, RhB, and phenol were used to assess the performance and adaptability of the $\text{CoFe}_2\text{O}_4\text{-Ag}_2\text{O}$ hybrids.

Adsorption of MO by different $\text{CoFe}_2\text{O}_4\text{-Ag}_2\text{O}$ samples in darkness was carried out to eliminate deviation. About 3% reduction in the initial MO concentration was observed after 40 min, with no further reduction observed after this. Thus, the time for adsorption in darkness was set at 40 min. After that, the photodegradation of MO by $\text{CoFe}_2\text{O}_4\text{-Ag}_2\text{O}$ samples with different Ag_2O contents under visible light irradiation was conducted; the results are shown in Fig. 5a.

The results confirm that the pure CoFe_2O_4 exhibits reaction inertness; MO concentration remains almost constant throughout the reaction period. However, with the addition of Ag_2O , MO can be completely decomposed within a few minutes. The photodegradation rate increases proportional to the increase in Ag_2O content. When the Ag_2O content of the $\text{CoFe}_2\text{O}_4\text{-Ag}_2\text{O}$ hybrid reached 80%, MO was completely decomposed in 5 min, which is equivalent to the reaction rate of pure Ag_2O . Thus, it was unnecessary to increase Ag_2O content further.

The graph in the inset of Fig. 5b shows that the relationship between $\ln(C/C_0)$ and irradiation time is linear. This means that the photocatalytic reaction with the $\text{CoFe}_2\text{O}_4\text{-Ag}_2\text{O}$ hybrids follows pseudo-first-order kinetics, which is in agreement with the common description of dye photodegradation models [8, 37, 38]. The value of the photoreaction rate constant, k , is equal to the corresponding slope of the fitting line. The relatively uniform increase of k with increasing Ag_2O content is shown in Fig. 5b. For the $\text{CoFe}_2\text{O}_4\text{-Ag}_2\text{O}$ (80%) hybrid, k reached 0.48 min^{-1} .

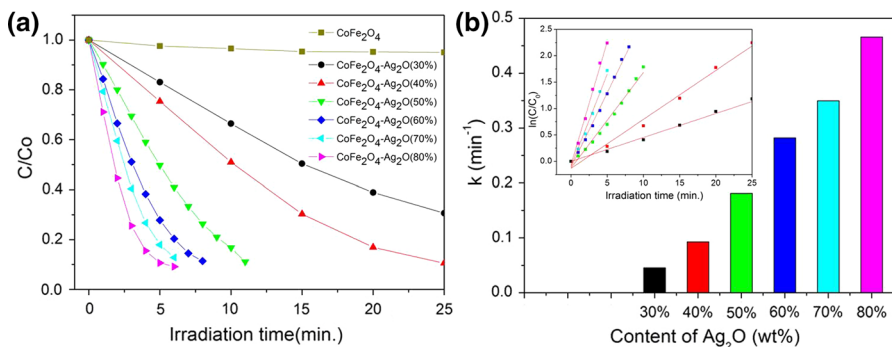


Fig. 5 **a** Effect of different catalysts on photocatalytic degradation of MO: $\text{CoFe}_2\text{O}_4\text{-Ag}_2\text{O}$ (mass content of Ag_2O from 30 to 80%). **b** The rate constant for the photodecomposition of MO on $\text{CoFe}_2\text{O}_4\text{-Ag}_2\text{O}$ photocatalysts with different Ag_2O content. The inset reveals the pseudo-first-order plots of $\ln(C/C_0)$ versus reaction time with the different Ag_2O content

Optimal Ag₂O content of CoFe₂O₄-Ag₂O

In this research, the purpose was to obtain a stable, magnetically separable Ag₂O photocatalyst with superb photocatalytic activity, the lowest viable Ag₂O content, and the highest magnetic recovery. Thus, the recyclability and reusability of the CoFe₂O₄-Ag₂O hybrids was investigated. The recovery rates and photocatalytic performances of CoFe₂O₄-Ag₂O (60%), CoFe₂O₄-Ag₂O (70%), and CoFe₂O₄-Ag₂O (80%) after five cycles were explored and the results are shown in Fig. 6.

As shown in Fig. 6, CoFe₂O₄-Ag₂O (60%) retained over 90% of its initial photocatalytic activity after 5 runs. MO was completely decomposed in 15 min during each run. No significant performance decline was observed, which suggests that CoFe₂O₄-Ag₂O (60%) possesses relatively excellent reusability and photocatalytic activities. The reusability of CoFe₂O₄-Ag₂O (70%) was poorer than that of CoFe₂O₄-Ag₂O (60%); after 5 runs, only 75% of the MO was decomposed in 15 min. CoFe₂O₄-Ag₂O (80%) displayed the worst reusability; 240 min were required for complete photodegradation of MO after 5 cycles. Despite the first run showing a very good photodegradation rate, the performance on cycling decreased too quickly for CoFe₂O₄-Ag₂O (80%) to be considered for further use.

Recyclabilities of the three samples after five runs were determined. The measured magnetic recovery rates of CoFe₂O₄-Ag₂O (60%), CoFe₂O₄-Ag₂O (70%), and CoFe₂O₄-Ag₂O (80%) in a magnetic field of 148.7 mT were 85.5, 73.8, and 43.3%, respectively, with these rates being achieved within 20 s. From this, it can be inferred that mass loss of photocatalyst could be the main factor of performance degradation of the hybrids. Considering the three key factors of performance degradation rate, photocatalytic performance stability, and Ag₂O usage, CoFe₂O₄-Ag₂O (60%) is the optimal hybrid for further application.

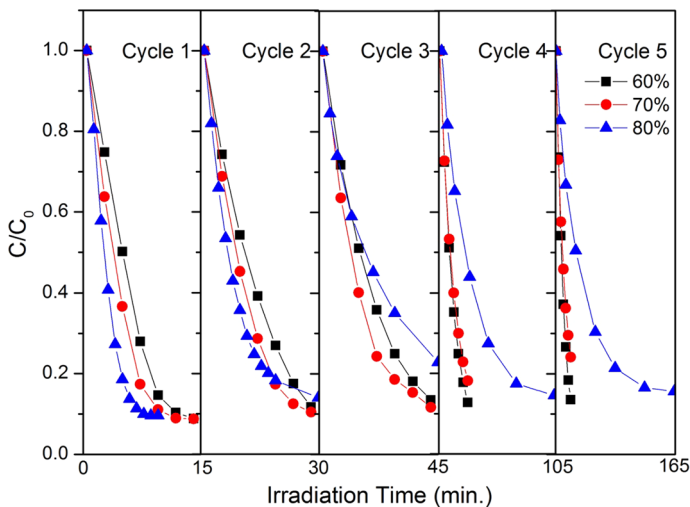


Fig. 6 Photodegradation of MO in the presence of magnetically recyclable CoFe₂O₄-Ag₂O (60%), CoFe₂O₄-Ag₂O (70%), and CoFe₂O₄-Ag₂O (80%) photocatalyst under visible light irradiation in cycles

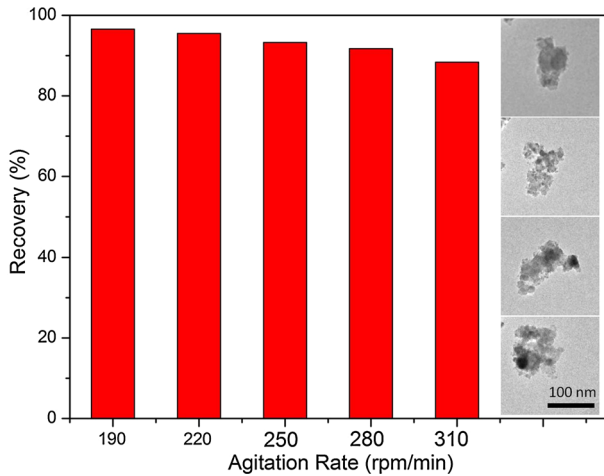


Fig. 7 Recoveries of CoFe₂O₄-Ag₂O (60%) with different agitation rates, and the TEM images of particles in liquid after magnetic separation

The stable photocatalytic performance and high recovery of CoFe₂O₄-Ag₂O (60%) should be ascribed to the maximum loading amount of Ag₂O on the surface of the CoFe₂O₄ support. If assuming the surface of the magnetic support has been completely covered by Ag₂O, the redundant Ag₂O only exists as the overlapping on loaded Ag₂O with weak adhesion, increasing the effective exposed active surface slightly. Thus, the photocatalytic performance upgrading of CoFe₂O₄-Ag₂O (70 and 80%) is limited, but their mass loss in recycling is significant.

This assumption can be confirmed by the determined magnetic recovery of CoFe₂O₄-Ag₂O composite against agitation rate. It can be noted that the magnetic recovery of CoFe₂O₄-Ag₂O shown in Fig. 7 has a slight decrease with the increase of the agitation intensity. The residue in the aqueous system after magnetic separation is nonmagnetic, and be determined as Ag₂O since the TEM images show its octahedron morphology. This result confirms that the detached material of CoFe₂O₄-Ag₂O composite is pure Ag₂O, and results in the performance decay and mass loss of CoFe₂O₄-Ag₂O.

Characterization of fresh and used CoFe₂O₄-Ag₂O (60%)

To investigate the reason for photocatalytic performance loss of the CoFe₂O₄-Ag₂O hybrid further, the components, morphology, and magnetic properties of CoFe₂O₄-Ag₂O (60%) before and after the photocatalysis process were characterized.

Figure 8a shows the XPS spectra of CoFe₂O₄-Ag₂O (60%) before and after five runs. No significant changes were observed in peak intensity or position, implying that there was no notable change in hybrid composition or any evidence of interaction. Detailed valence state analyses of Ag 3d, Co 2p, and Fe 2p were conducted; Figs. 8b, 6c, d show the narrow scan spectra, respectively. As seen in Fig. 8b, there are two independent peaks at 368.2 and 374.1 eV, which can be

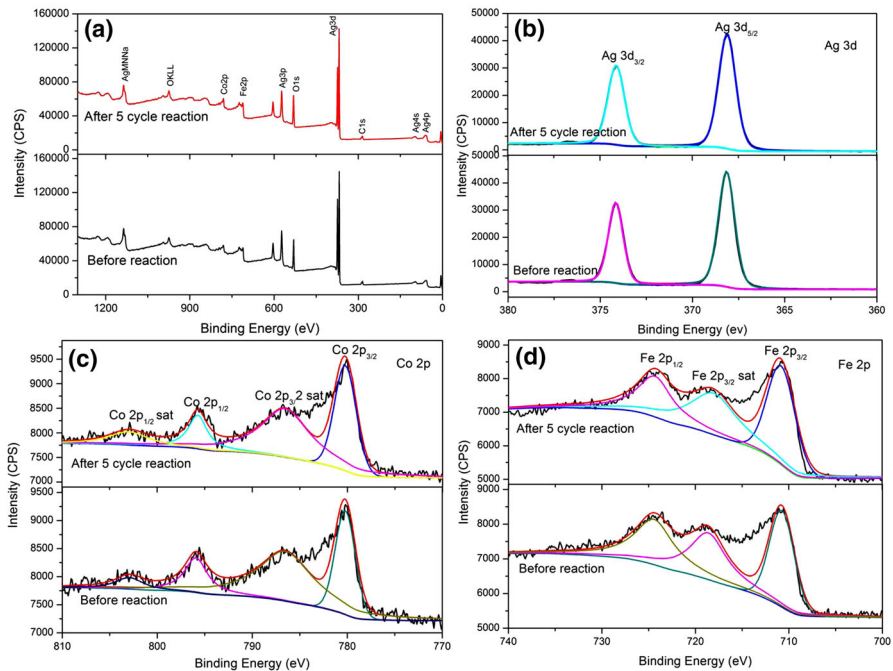


Fig. 8 a XPS wide spectrum of $\text{CoFe}_2\text{O}_4\text{-Ag}_2\text{O}$ (60%). Decomposed XPS b Ag 3d, c Fe 2p, and d Co 2p

assigned to $\text{Ag } 3d_{5/2}$ and $\text{Ag } 3d_{3/2}$ of Ag^+ , respectively [39]. The Ag valence state exhibits no change after five cycles, implying the excellent stability of the Ag_2O active component in the $\text{CoFe}_2\text{O}_4\text{-Ag}_2\text{O}$ (60%) hybrid.

The main peaks of the Co 2p spectrum (Fig. 8c) are at 796.2 and 785.0 eV and are assigned to $\text{Co } 2p_{1/2}$ and $\text{Co } 2p_{3/2}$, respectively; the other two peaks at 802.8 and 786.0 eV are attributed to the two orbitals' shake-up satellite peaks [40]. The Fe 2p spectrum (Fig. 8d) shows peaks at 724.4 and 711.3 eV that are assigned to $\text{Fe } 2p_{1/2}$ and $\text{Fe } 2p_{3/2}$ [41], respectively, and a peak at 718.8 eV that is assigned to the shake-up satellite of $\text{Fe } 2p_{3/2}$ [42]. The inertness of the magnetic support in $\text{CoFe}_2\text{O}_4\text{-Ag}_2\text{O}$ (60%) during the photocatalytic process was confirmed by the Co 2p and Fe 2p peaks remaining unchanged. The above XPS results show that the components of $\text{CoFe}_2\text{O}_4\text{-Ag}_2\text{O}$ (60%) remained stable during the photocatalysis process.

The hysteresis loops of $\text{CoFe}_2\text{O}_4\text{-Ag}_2\text{O}$ (60%) measured at 300 K before and after reaction are shown in Fig. 9a. The two hysteresis loops approximately overlap, showing ferromagnetic behavior at room temperature [43]. A slight decrease of saturation magnetization of $\text{CoFe}_2\text{O}_4\text{-Ag}_2\text{O}$ (60%) was observed from 22.45 emu g^{-1} initially to 22.24 emu g^{-1} after 5 runs, which can be ascribed to testing error. As shown in Fig. 9b, such slight deviation does not significantly influence the magnetic recovery rate; the recovery rate for $\text{CoFe}_2\text{O}_4\text{-Ag}_2\text{O}$ (60%) was 92.38% after the third magnetic process in a magnetic field of 148.7 mT, although in the first and second separations, the recovery rates were 96.37 and

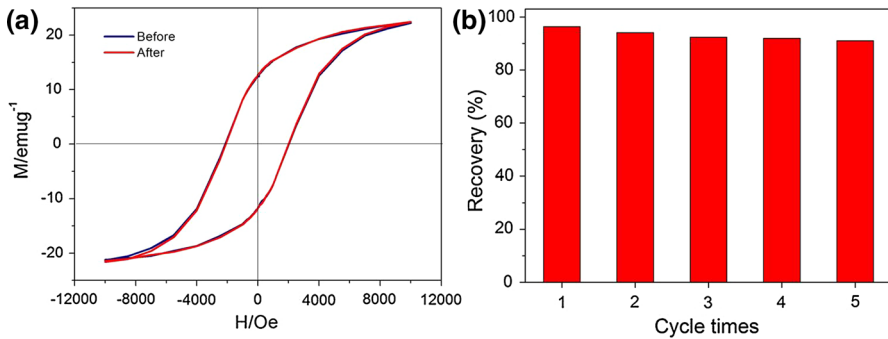


Fig. 9 **a** Magnetic hysteresis loop of as-prepared $\text{CoFe}_2\text{O}_4\text{-Ag}_2\text{O}$ (60%) and after five runs. **b** Recovery of five times

94.10%, respectively. The residue after magnetic recovery was determined to be pure Ag_2O . This may be the reason for the performance degradation because the quantity of Ag_2O loaded on the magnetic support decreases on cycling. However, this relatively high recovery percentage confirmed that the introduction of a magnetic support could effectively solve the problem of Ag_2O nanoparticles, saving cost and avoiding possible pollution.

The detachment of Ag_2O was confirmed by the SEM images before and after five runs, as shown in Fig. 10a, b. It was observed that some of the protruded structures on the fresh sample disappear after cycling, which suggests that Ag_2O has dissociated from the support. The BET analysis confirmed that the surface area of the cycled $\text{CoFe}_2\text{O}_4\text{-Ag}_2\text{O}$ (60%) hybrid decreased to $21.3218 \text{ m}^2 \text{ g}^{-1}$, which can be ascribed to the loss of Ag_2O nanoparticles. Thus, it can be ascertained that it is the loss of free Ag_2O content that results in the slight performance degradation of $\text{CoFe}_2\text{O}_4\text{-Ag}_2\text{O}$ (60%).

Electronic structure was also investigated with UV-Vis DRS and PL analysis. The determined band gap of the cycled $\text{CoFe}_2\text{O}_4\text{-Ag}_2\text{O}$ (60%) was the same as before cycling (Fig. 10c), which verifies its unchanged electronic structure. However, PL analysis exhibited a marked increase in fluorescence intensity after five runs (Fig. 10d); this suggests an increase in the recombination rate of photo-generated electrons and holes, which is in agreement with the slight decrease in photodegradation rate observed.

Therefore, it is concluded that the combined effect of mass loss and quantum efficiency decrease in loaded Ag_2O caused the performance degradation of $\text{CoFe}_2\text{O}_4\text{-Ag}_2\text{O}$ (60%). However, the stability of $\text{CoFe}_2\text{O}_4\text{-Ag}_2\text{O}$ (60%) is still relatively attractive for actual application.

Extensive application of $\text{CoFe}_2\text{O}_4\text{-Ag}_2\text{O}$ (60%)

While $\text{CoFe}_2\text{O}_4\text{-Ag}_2\text{O}$ (60%) has shown excellent photocatalytic performance, stability, and magnetic recovery rate for decomposing MO, it is necessary to investigate whether it can degrade other organic pollutants. MB, RhB, and phenol

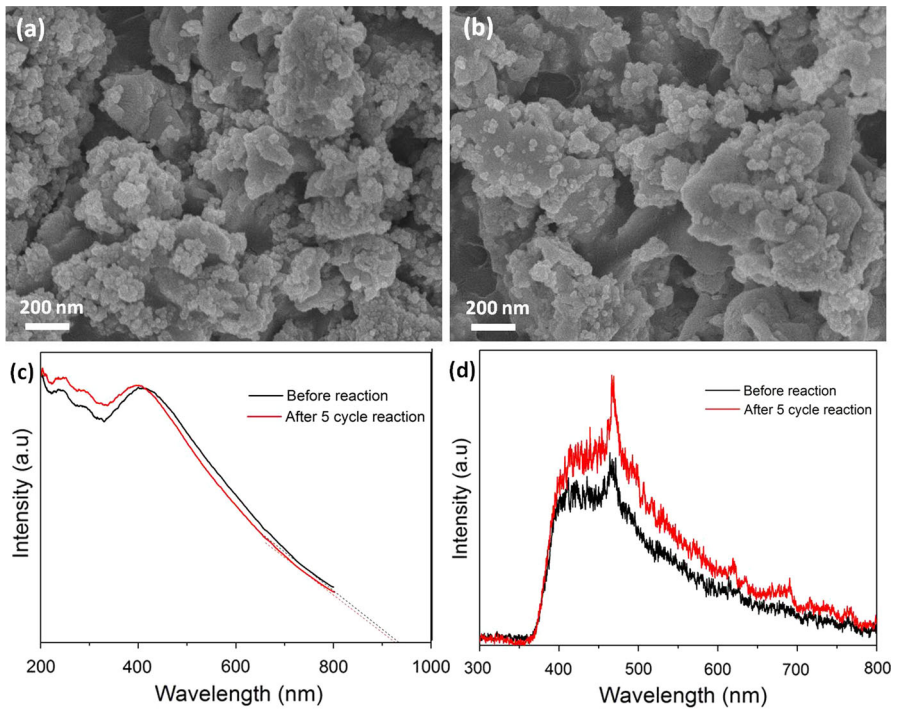


Fig. 10 SEM images (a, b), UV-Vis (c) and PL (d) of fresh $\text{CoFe}_2\text{O}_4\text{-Ag}_2\text{O}$ (60%) and after five cycles of reaction

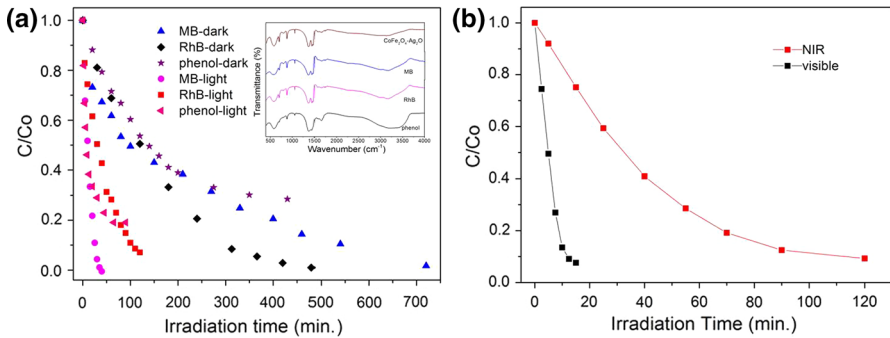


Fig. 11 a The degradation rate of MB, RhB, and phenol in darkness and under visible light irradiation. The inset reveals the Fourier-transform infrared (FT-IR) spectra of $\text{CoFe}_2\text{O}_4\text{-Ag}_2\text{O}$ (60%) hybrid (post-photodegradation). b Photodegradation of MO in the presence of $\text{CoFe}_2\text{O}_4\text{-Ag}_2\text{O}$ (60%) under visible light and near-infrared (NIR) light

were selected to evaluate the performance of $\text{CoFe}_2\text{O}_4\text{-Ag}_2\text{O}$ (60%). Results are shown in Fig. 11.

Figure 11a shows that all of MB and RhB, and ~30% of phenol, are adsorbed in the dark within 12, 8, and 7 h, respectively, which is a much stronger adsorption

response than observed for the MO. Such strong adsorption could be ascribed to the large surface area of $\text{CoFe}_2\text{O}_4\text{-Ag}_2\text{O}$ (60%), since the adsorption on pure Ag_2O with low surface area is small, with negative ζ -potential, due to MB and RhB being cationic dyes [44, 45]. Photodegradation occurred even on exposure to visible light without an adsorption phase, with MB, RhB, and phenol being completely decomposed in 30 min, 120 min, and 50 min, respectively. Fourier-transform infrared spectra (inset in Fig. 11a) confirmed that the adsorbed organics can be decomposed under light irradiation. This confirms that the strong adsorption plays a positive role in the photocatalytic process because it can enrich the soluble organics on the surface of the photocatalyst. Overall, $\text{CoFe}_2\text{O}_4\text{-Ag}_2\text{O}$ (60%) shows excellent photocatalytic activity for degrading MB, RhB, and phenol, thereby confirming its wide applicability.

MO photodegradation was also carried out under near-infrared (NIR) light irradiation to verify the photocatalytic ability over a wider spectrum including longer wavelengths. Figure 11b shows that the MO was completely decomposed in 120 min under NIR illumination. Although the photodegradation rate is slower, this shows that $\text{CoFe}_2\text{O}_4\text{-Ag}_2\text{O}$ (60%) works over a wider spectrum than traditional photocatalysts, such as TiO_2 . This attractive property can be ascribed to the narrow band gap of Ag_2O .

Conclusion

In this research, a range of magnetically separable $\text{CoFe}_2\text{O}_4\text{-Ag}_2\text{O}$ hybrid photocatalysts of different Ag_2O contents were prepared and evaluated. $\text{CoFe}_2\text{O}_4\text{-Ag}_2\text{O}$ hybrids exhibited excellent photocatalytic performance under visible light and NIR light irradiation. Typical persistent organics, such as MO, MB, RhB, and phenol, were completely photodecomposed with the optimized hybrid $\text{CoFe}_2\text{O}_4\text{-Ag}_2\text{O}$ (60%) within 120 min. This hybrid photocatalyst can be effectively separated magnetically without considerable mass loss, and can be reused without significant performance degradation. This excellent photocatalytic performance and separation recovery confirms that the $\text{CoFe}_2\text{O}_4\text{-Ag}_2\text{O}$ photocatalyst is a promising compound for future application for photo-oxidative degradation of organic contaminants.

Acknowledgements We are thankful for the financial support provided by the National Natural Science Foundation of China Project (no. 21476146).

References

1. M.N. Chong, B. Jin, C.W. Chow, C. Saint, Recent developments in photocatalytic water treatment technology: a review. *Water Res* **44**, 2997–3027 (2010)
2. M.F.R. Pereira, S.F. Soares, J.J.M. Órfão, J.L. Figueiredo, Adsorption of dyes on activated carbons: influence of surface chemical groups. *Carbon* **41**, 811–821 (2003)
3. S. Wang, Y. Boyjoo, A. Choueib, Z.H. Zhu, Removal of dyes from aqueous solution using fly ash and red mud. *Water Res* **39**, 129–138 (2005)
4. Z. Aksu, Application of biosorption for the removal of organic pollutants: a review. *Process Biochem* **40**, 997–1026 (2005)

5. Z. Du, H. Li, T. Gu, A state of the art review on microbial fuel cells: a promising technology for wastewater treatment and bioenergy. *Biotechnol Adv* **25**, 464–482 (2007)
6. G. Chen, Electrochemical technologies in wastewater treatment. *Sep Purif Technol* **38**, 11–41 (2004)
7. A.L. Linsebigler, G. Lu, J.T. Yates, Photocatalysis on TiO₂ surfaces: principles, mechanisms, and selected results. *Chem Rev* **95**, 735–758 (1995)
8. I.K. Konstantinou, T.A. Albanis, TiO₂-assisted photocatalytic degradation of azo dyes in aqueous solution: kinetic and mechanistic investigations. *Appl Catal B Environ* **49**, 1–14 (2004)
9. A. Fujishima, X. Zhang, D. Tryk, Heterogeneous photocatalysis: from water photolysis to applications in environmental cleanup. *Int J Hydrogen Energy* **32**, 2664–2672 (2007)
10. D. Chatterjee, S. Dasgupta, Visible light induced photocatalytic degradation of organic pollutants. *J Photochem Photobiol, C* **6**, 186–205 (2005)
11. R. Murugan, V.J. Babu, M.M. Khin, A.S. Nair, S. Ramakrishna, Synthesis and photocatalytic applications of flower shaped electrospun ZnO–TiO₂ mesostructures. *Mater Lett* **97**, 47–51 (2013)
12. J. Zhang, Q. Xu, Z. Feng, M. Li, C. Li, Importance of the relationship between surface phases and photocatalytic activity of TiO₂. *Angew Chem* **47**, 1766–1769 (2008)
13. Y. Gai, J. Li, S.S. Li, J.B. Xia, S.H. Wei, Design of narrow-gap TiO₂: a passivated godoping approach for enhanced photoelectrochemical activity. *Phys Rev Lett* **102**, 3–23 (2009)
14. Y. Bi, S. Ouyang, N. Umezawa, J. Cao, J. Ye, Facet effect of single-crystalline Ag₃PO₄ sub-microcrystals on photocatalytic properties. *J Am Chem Soc* **133**, 6490–6492 (2011)
15. Z. Yi, J. Ye, N. Kikugawa, T. Kako, S. Ouyang, H. Stuart-Williams, H. Yang, J. Cao, W. Luo, Z. Li, An orthophosphate semiconductor with photooxidation properties under visible-light irradiation. *Nat Mater* **9**, 559–564 (2010)
16. W. Jiang, Y. Zeng, X. Wang, X. Yue, S. Yuan, H. Lu, B. Liang, Preparation of silver carbonate and its application as visible light-driven photocatalyst without sacrificial reagent. *Photochem Photobiol* **91**, 1315–1323 (2015)
17. H. Dong, G. Chen, J. Sun, C. Li, Y. Yu, D. Chen, A novel high-efficiency visible-light sensitive Ag₂CO₃ photocatalyst with universal photodegradation performances: simple synthesis, reaction mechanism and first-principles study. *Appl Catal B Environ* **134–135**, 46–54 (2013)
18. G. Dai, J. Yu, G. Liu, A new approach for photocorrosion inhibition of Ag₂CO₃ photocatalyst with highly visible-light-responsive reactivity. *J Phys Chem C* **116**, 15519–15524 (2012)
19. J. Tang, Y. Liu, H. Li, Z. Tan, D. Li, A novel Ag₃AsO₄ visible-light-responsive photocatalyst: facile synthesis and exceptional photocatalytic performance. *Chem Commun* **49**, 5498 (2013)
20. J. Zhou, Y. Cheng, J. Yu, Preparation and characterization of visible-light-driven plasmonic photocatalyst Ag/AgCl/TiO₂ nanocomposite thin films. *J Photochem Photobiol, A* **223**, 82–87 (2011)
21. C. Hu, Y. Lan, J. Qu, X. Hu, A. Wang, Ag/AgBr/TiO₂ visible light photocatalyst for destruction of azodyes and bacteria. *J Phys Chem B* **110**, 4066–4072 (2006)
22. H. Cheng, B. Huang, Y. Dai, X. Qin, X. Zhang, One-step synthesis of the nanostructured AgI/BiOI composites with highly enhanced visible-light photocatalytic performances. *Langmuir* **26**, 6618–6624 (2010)
23. W. Jiang, Z. Wu, X. Yue, S. Yuan, H. Lu, B. Liang, Photocatalytic performance of Ag₂S under irradiation with visible and near-infrared light and its mechanism of degradation. *RSC Adv* **5**, 24064–24071 (2015)
24. W. Jiang, X. Wang, Z. Wu, X. Yue, S. Yuan, H. Lu, B. Liang, Silver oxide as superb and stable photocatalyst under visible and near-infrared light irradiation and its photocatalytic mechanism. *Ind Eng Chem Res* **54**, 832–841 (2015)
25. X. Wang, S. Li, H. Yu, J. Yu, S. Liu, Ag₂O as a new visible-light photocatalyst: self-stability and high photocatalytic activity. *Chem Eur J* **17**, 7777–7780 (2011)
26. S. Shylesh, V. Schünemann, W.R. Thiel, Magnetically separable nanocatalysts: bridges between homogeneous and heterogeneous catalysis. *Angew Chem Int Edit* **49**, 3428–3459 (2010)
27. X. Cui, Y. Li, Q. Zhang, H. Wang, Silver orthophosphate immobilized on flaky layered double hydroxides as the visible-light-driven photocatalysts. *Int J Photoenergy* **2012**, 1–6 (2012)
28. J.M. Campelo, D. Luna, R. Luque, J.M. Marin, Sustainable preparation of supported metal nanoparticles and their applications in catalysis. *ChemSusChem* **2**, 18–45 (2009)
29. P. Chaus, A. Brückner, C. Mohr, H. Hofmeister, Supported gold nanoparticles from quantum dot to mesoscopic size scale: effect of electronic and structural properties on catalytic hydrogenation of conjugated functional groups. *J Am Chem Soc* **122**, 11430–11439 (2000)
30. Y. Fu, H. Chen, X. Sun, X. Wang, Combination of cobalt ferrite and graphene: high-performance and recyclable visible-light photocatalysis. *Appl Catal B Environ* **111–112**, 280–287 (2012)

31. L. Chen, W. Ma, J. Dai, J. Zhao, C. Li, Y. Yan, Facile synthesis of highly efficient graphitic-C₃N₄/ZnFe₂O₄ heterostructures enhanced visible-light photocatalysis for spiramycin degradation. *J Photochem Photobiol, A* **328**, 24–32 (2016)
32. S. Rana, J. Rawat, R.D.K. Misra, Anti-microbial active composite nanoparticles with magnetic core and photocatalytic shell: TiO₂-NiFe₂O₄ biomaterial system. *Acta Biomater* **1**, 691–703 (2005)
33. H. Zhang, J. Wang, S.E. Lofland, Z. Ma, L. Mohaddes-Ardabili, T. Zhao, L. Salamanca-Riba, S.R. Shinde, S.B. Ogale, F. Bai, D. Viehland, Y. Jia, D.G. Schlom, M. Wuttig, A. Roytburd, R. Ramesh, Multiferroic BaTiO₃-CoFe₂O₄ nanostructures. *Science* **303**, 661–663 (2004)
34. H.A.J.L. Mourão, A.R. Malagutti, C. Ribeiro, Synthesis of TiO₂-coated CoFe₂O₄ photocatalysts applied to the photodegradation of atrazine and rhodamine B in water. *Appl Catal A Gen* **382**, 284–292 (2010)
35. C. Borgohain, K.K. Senapati, K.C. Sarma, P. Phukan, A facile synthesis of nanocrystalline CoFe₂O₄ embedded one-dimensional ZnO hetero-structure and its use in photocatalysis. *J Mol Catal A: Chem* **363–364**, 495–500 (2012)
36. Z. Szotek, W.M. Temmerman, D. Ködderitzsch, A. Svane, L. Petit, H. Winter, Electronic structures of normal and inverse spinel ferrites from first principles. *Phys Rev B* **74**, 174431 (2006)
37. Y. Li, X. Li, J. Li, J. Yin, Photocatalytic degradation of methyl orange by TiO₂-coated activated carbon and kinetic study. *Water Res* **40**, 1119–1126 (2006)
38. H. Lachheb, E. Puzenat, A. Houas, M. Ksibi, E. Elaloui, C. Guillard, J. Herrmann, Photocatalytic degradation of various types of dyes (Alizarin S, Crocein Orange G, Methyl Red, Congo Red, Methylene Blue) in water by UV-irradiated titania. *Appl Catal B Environ* **39**, 75–90 (2002)
39. G.B. Hoflund, Z.F. Hazos, Surface characterization study of Ag, AgO, and Ag₂O using x-ray photoelectron spectroscopy and electron energy-loss spectroscopy. *Phys Rev B* **62**, 11126–11133 (2000)
40. G. Wang, Y. Ma, Z. Wei, M. Qi, Development of multifunctional cobalt ferrite/graphene oxide nanocomposites for magnetic resonance imaging and controlled drug delivery. *Chem Eng J* **289**, 150–160 (2016)
41. S.J. Roosendaal, B. van Asselen, J.W. Elsenaar, A.M. Vredenberg, F.H.P.M. Habraken, *Surf Sci* **442**, 329–337 (1990)
42. T. Yamashita, P. Hayes, Analysis of XPS spectra of Fe²⁺ and Fe³⁺ ions in oxide materials. *Appl Surf Sci* **254**, 2441–2449 (2008)
43. E. Mazario, P. Herrasti, M.P. Morales, N. Menendez, Synthesis and characterization of CoFe₂O₄ ferrite nanoparticles obtained by an electrochemical method. *Nanotechnology* **23**, 355708 (2012)
44. M. Ge, N. Zhu, Y. Zhao, J. Li, L. Liu, Sunlight-assisted degradation of dye pollutants in Ag₃PO₄ suspension. *Ind Eng Chem Res* **51**, 5167–5173 (2012)
45. L.-M. Lyu, M.H. Huang, Investigation of relative stability of different facets of Ag₂O nanocrystals through face-selective etching. *J Phys Chem C* **115**, 17768–17773 (2011)